Experimental and numerical investigation into rolling contact fatigue crack initiation on the V-Track test rig

Ren, Fang; Yang, Zhen; Li, Zili

DOI
10.1016/j.engfailanal.2024.109206

Publication date
2025

Document Version
Final published version

Published in
Engineering Failure Analysis

Citation (APA)
Ren, F., Yang, Z., & Li, Z. (2025). Experimental and numerical investigation into rolling contact fatigue crack initiation on the V-Track test rig. *Engineering Failure Analysis*, *170*, Article 109206. https://doi.org/10.1016/j.engfailanal.2024.109206

Engineering Failure Analysis 170 (2025) 109206

Contents lists available at ScienceDirect

Engineering Failure Analysis

journal homepage: www.elsevier.com/locate/engfailanal

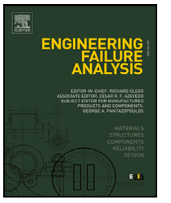

Experimental and numerical investigation into rolling contact fatigue crack initiation on the V-Track test rig

Fang Ren, Zhen Yang, Zili Li *

Delft University of Technology, Stevinweg 1, 2628 CN, Delft, The Netherlands

ARTICLE INFO

Keywords:
Rolling contact fatigue
Ratcheting
Microscopic analysis
Finite element analysis

ABSTRACT

This study experimentally and numerically investigated wheel–rail rolling contact fatigue (RCF), focusing on the initiation mechanisms of head check (HC). The experimental study was conducted using V-Track, a scaled test rig developed at TU Delft that is able to simulate real-life wheel–rail contact with controllable contact geometries and loading conditions. Ratcheting and HCs were generated on the V-Track rails with wheel–rail frictional rolling contact loading for up to 60,000 cycles. Rail samples with HCs were then examined with a microscopic analysis focusing on the R260MN steel grade. The boundary element method (BEM) and finite element method (FEM) were then applied to calculate wheel–rail contact-induced stress states in and below the rail surface under the same contact conditions as the experiment. The rail surface shear stresses calculated with BEM exhibited a strong correlation to the ratcheting observed within the rail running band in the microscopic analysis. Moreover, the plastic flows and cracks outside the running band identified by the microscopic analysis were correlated to the rail surface stresses, especially outside the contact patch, and subsurface stresses calculated with FEM: the results suggested that the accumulation of residual stresses could also contribute to plastic flow and the consequent initiation of cracks outside the running band.

1. Introduction

Head check (HC), a typical type of rolling contact fatigue (RCF), has been a persistent issue for modern railways. The HC damage is characterised as groups of regularly spaced cracks that appear in the rail head. Once the cracks initiate, they can propagate [1,2], leading to shelling or forced fracture of rails [3]. Grinding has been widely used as a means to control the damage, whereas its cost effectiveness remains a challenge in terms of the timing and extent of material removal or even rail replacement. Untimely or inadequate treatment of HC damage may cause substantial economic consequences and even fatal accidents [4]. To avoid these, an accurate prediction of HC crack initiation is desirable.

Multiple factors have been found to contribute to the initiation of HC. HC cracks are generally observed on curves [5–7], where lateral creep force introduced by the curving behaviour of bogie causes the shift of contact from rail top towards gauge corner. Large geometrical spin then rises when the wheel flange root with large conicity comes into contact with the rail shoulder or gauge corner. The large shear stresses induced by the lateral creep force and geometrical spin contribute to the initiation of HC [5]. Furthermore, under the cyclic loading that is essential for material fatigue problems, ratcheting, i.e. the directional plastic strain accumulation [8], occurs when the plastic shakedown limit is exceeded [9]. Cracks can initiate within the layer of plastic deformation following the direction of plastic flow [10] when the ratcheting reaches a critical level [11].

* Corresponding author.
E-mail address: Z.Li@tudelft.nl (Z. Li).

https://doi.org/10.1016/j.engfailanal.2024.109206
Received 8 October 2024; Received in revised form 3 December 2024; Accepted 14 December 2024

Available online 21 December 2024

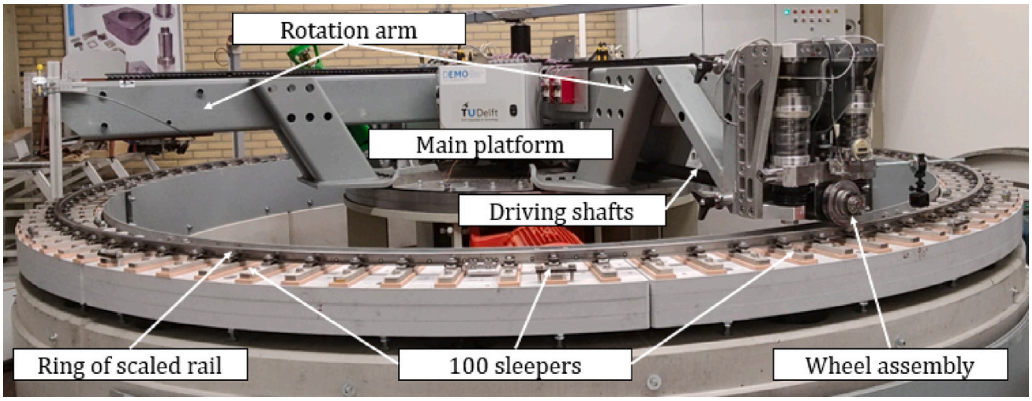

Fig. 1. The V-Track test rig.

To investigate the mechanisms of RCF damage including HC, various tests have been conducted to generate RCF. Twin-disc tests have been widely used to replicate the frictional rolling contacts, resulting in clusters of RCF cracks [12–16]. The twin-disc tests offer the advantages of easy setup and control of test parameters, e.g., allowing for the adjustment of rotational velocity and alignment of the discs to control and monitor the longitudinal [13] and lateral creepage [17]. RCF cracks, HC in particular, have also been generated on the Voestalpine test rig [5,6,18], consisting of a full-scale wheel and a 1.5-m-long straight rail in reciprocating motion at the maximum speed of 0.5 m/s [6]. This test rig can apply vertical and lateral loads on the test track without longitudinal traction force [19]. Nonetheless, the twin-disc test rigs might not properly represent the hardness of a head-hardened rail due to the ways the discs/rollers were manufactured [7,20], while the full-scale, e.g. Voestalpine, test rigs have limitations in terms of operational speed, accurate control of wheel–rail contact loading conditions, and potentially high costs. Furthermore, none of the aforementioned test rigs can simultaneously test rail samples with different materials. It has been reported that the head-hardened rail exhibits greater resistance to RCF [6], and new rail steel materials such as bainitic steel possess improved mechanical properties [21]. To efficiently investigate the effects of material properties on RCF initiation under a large number of load cycles, a test rig capable of simultaneously testing multiple rail materials is desirable.

In this study, the V-Track test rig [22] was employed to produce HC crack initiation under controlled and monitored loading conditions. This scaled test rig was developed by the Section of Railways Engineering at TU Delft for the study of vehicle–track interaction with frictional rolling contact. Compared to the twin-disc tests, the V-Track rails, when extracted from the head-hardened real-life rails, can accurately represent the hardness distribution in the rail head. The contact geometry can be flexibly controlled by using customised profiles of rail and wheel [23,24]. Moreover, multiple rail steel grades can be incorporated into one setup and tested simultaneously, facilitating the study of HC crack initiation and propagation in different rail steels. Applying the same loading condition and contact geometry as in the V-Track test, this study then numerically analysed wheel–rail contact-induced stress states on the rail surface and subsurface with the boundary element method (BEM) and the FEM. The BEM [5,18,25] is favoured for its rapid and accurate rolling contact solutions, but limited by the assumption of linear elasticity and cannot address the stress states beyond the contact patch. The FEM is thus employed complementarily. To investigate the mechanisms of HC initiation, the numerical solutions were then correlated to the V-Track rail cracks and plastic flow patterns observed via a microscopic analysis.

2. Methodology

2.1. HC test

2.1.1. V-Track test rig

Fig. 1 shows the V-Track test rig that was used to generate HC damage in this study. It features compact and lightweight rails and wheels, and is thus convenient for sample cutting for the further microscopic analysis. The scaled rails were bent to form the ring track, which is with a radius of 2 metres and supported by 100 steel sleepers. In this study, four steel grades were tested simultaneously, each spanning over 25 sleepers. The tested grades include three pearlitic steels: R220, R260MN, MHH, and one bainitic steel: B320. The grades B320 (on sleepers NO.1–25), R220 (on sleepers NO. 26–50) and R260MN (on sleepers NO. 51–75) are naturally hard steels, while the grade MHH (on sleepers NO. 76–100) is head-hardened. The R260MN and MHH were selected due to their wide application in Dutch railways, while the inclusion of R220 and B320 aimed to examine the competing effects of RCF and wear on softer rail steel [6,26] and to improve knowledge on the RCF resistance of bainitic steel, respectively. This study focused on the R260MN rails on V-Track.

The V-Track can accommodate four wheel assemblies for testing, each equipped with multiple sensors capable of measuring wheel/rail dynamic responses and contact forces at the wheel–rail interface. The wheel assemblies are driven by rotation arms of the main platform and can run at a speed of up to 40 km/h. The wheels can also be connected to an actuation motor via driving shafts. The torque applied to the wheel through the driving shaft can produce traction or braking force, and thus the longitudinal creepage, at the wheel–rail interface to simulate wheel–rail contact under desired traction conditions.

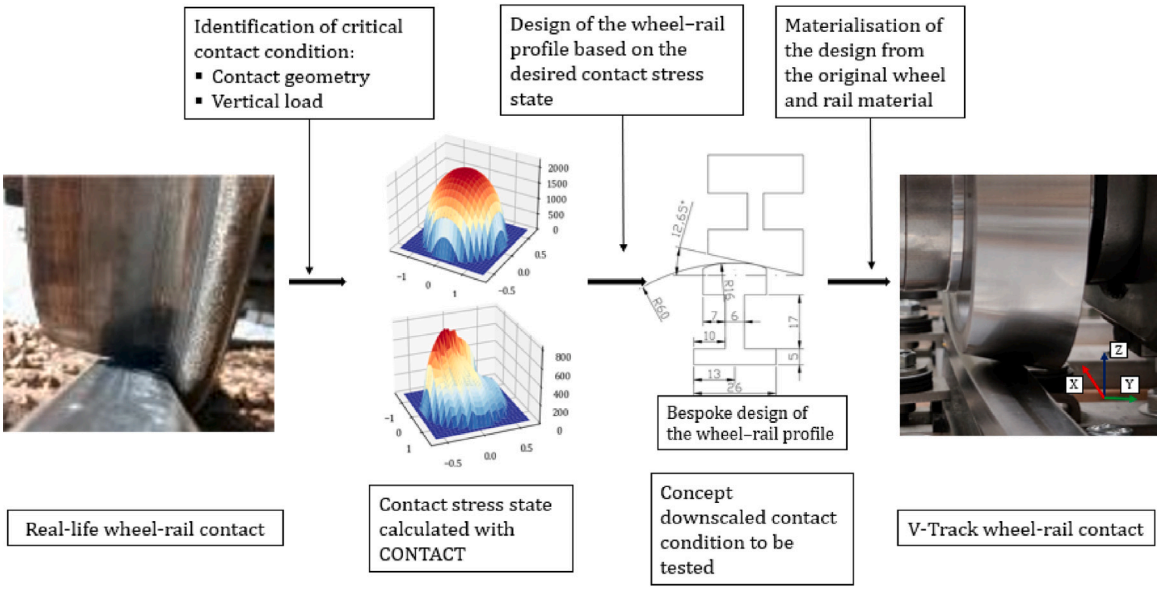

Fig. 2. The scale wheel and rail design process for V-Track.

2.1.2. Contact geometry

For the HC generation in this study, the wheel and rail profiles of the V-Track were carefully designed and customised to reproduce real-life wheel–rail contact geometries at locations prone to HC damage, such as the rail shoulders and gauge corners [6,7,19]. The wheel and rail profiles used in this study and their design process are presented in Fig. 2. The CONTACT program [25] was used to match the contact stress conditions between the scaled and real-life contact geometries as indicated in Fig. 2. Geometrical spin was also introduced by adopting a conical wheel profile to study its influence on the initiation of HC, as suggested by [5]. Unlike the real-life wheels with certain curved profiles (e.g. S1002), the V-Track wheels applied in this study were fabricated with constant conicity to simplify the loading condition control and to facilitate the comparison between the measurement and numerical simulation results.

The scaled wheels and rails used in V-Track were carefully fabricated from the original materials as indicated in Fig. 3. Fig. 3(a) shows that scaled rails were cut at 1 mm below the original rail head surface to capture the hardness close to contact interface. This practise is particularly crucial for the head-hardened MHH steel grade due to its inhomogeneously distributed hardness in rail head [7,20]. The scaled wheels were made from the tread of the original wheel with their contact surface close to the original contact locations on tread and flange as shown in Fig. 3(b)

2.1.3. Loading condition

The loading conditions were also controlled to closely mimic the real-life wheel–rail contact during curving. The normal Hertzian contact stress of about 2 GPa that matches the previous research on HC initiation [19] was used in this study to produce plastic deformation and ratcheting. Based on the designed contact geometry, the vertical load of 3500N was determined. To simulate a driving wheel, a positive wheel torque was applied in the test, resulting in a steady-state traction force and an average traction coefficient (traction force over normal contact force) of 0.17, with some variation in the forces from dynamic effects (see in Fig. 5 of Section 3.1). The presence of wheel conical angle of 12.65 degrees [19] led to geometrical spin and a lateral frictional force of about 250 N. The average coefficient of adhesion was approximately 0.22, which is the resultant friction forces (traction and lateral forces) divided by normal contact force. The measured time histories of the wheel–rail contact loads can be found in Section 3.1.

2.2. Numerical analysis

Numerical analyses were performed in this study at two stages. At the first stage, a BEM analysis was performed using the CONTACT program [25] to estimate the rail surface stress state within the wheel–rail contact patch. The wheel–rail contact loads measured from the V-Track were used as the inputs for the CONTACT program. The contact patch size, magnitude of the normal and shear stresses, and orientation of the surface shear stresses can then be calculated.

Since the CONTACT program is limited by assuming linear elasticity and the solutions are constrained within the contact patch on the contact surface, FEM was employed at the second stage to investigate the stress states on the rail surface beyond the wheel–rail contact patch and beneath the rail surface with considerations of nonlinear material properties (as elaborated in Section 3.5). The FEM has been proven to be reliable for solving wheel–rail contact problems [27,28] incorporating material plasticity [29–31], which is critical for the analysis of RCF.

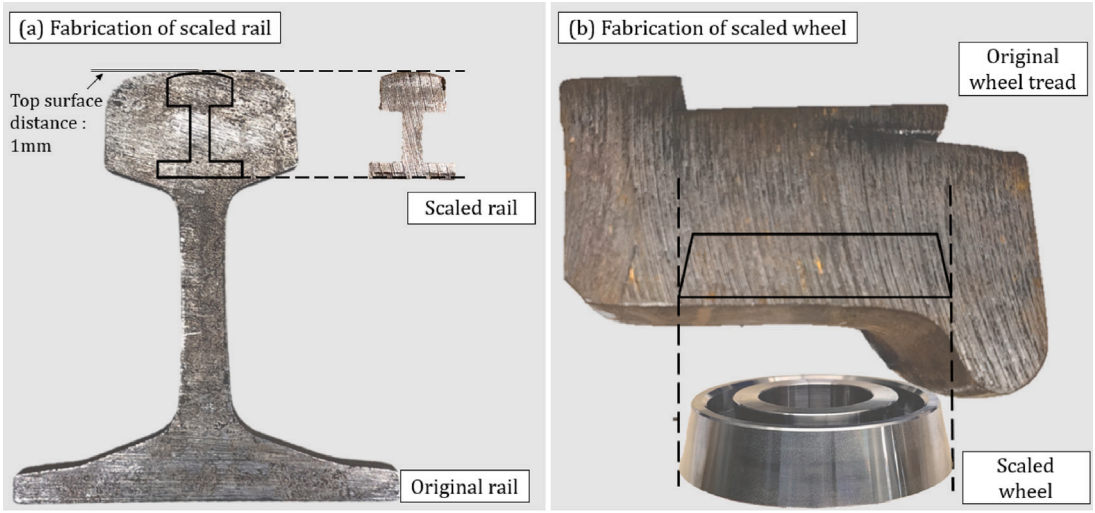

Fig. 3. Fabrication of scale wheel and rail: (a) scaled rail from the original rail profile, and (b) scaled wheel from the original wheel tread.

Two finite element (FE) models were built in this study to calculate the rail surface contact and subsurface stress states over the first cycle of rolling contact, with its FE modelling procedure verified in [32]. The first model duplicated the conical wheel–rail contact at the V-Track test rig (see Fig. 2) with the same loading condition measured at sleeper NO. 72. The second model simulated the contact between a cylindrical wheel and a rail with the radius of the wheel matching the exact contact radius of the conical wheel. By comparing the results obtained with the two models, the effects of wheel conicity and consequent geometrical spin can be identified. In both FE models, the wheels were modelled with elastic material. The elastic material was first used in the rail model to identify subsurface stress patterns and verify surface contact stresses against CONTACT solutions. Subsequently, the BLKH material was applied in the rails of both FE models to examine the distribution of (residual) stresses in the rail during and after the contact. The BLKH material was represented by an elastic part with a Young's modulus of 200 GPa and a yield stress of 500 MPa, and a plastic part with a plastic modulus of 14 GPa for stress values above the yield stress.

2.3. Microscopic analysis

Microscopic analysis was performed to examine the plastic deformation and crack initiation induced by rolling contact. The rail samples were selected following the observation of surface damage and cut from the tested R260MN steel grades from the V-Track. Since R260MN is one of the most widely used steel grades in the Netherlands, priority was given to it in our microscopic analysis of this study, with the rest of the steel grades to be processed. Two types of rail head samples were prepared: the longitudinal and transverse samples, as shown in Fig. 4. Two longitudinal samples were cut along the wheel running direction based on the findings from surface observation (to be discussed in Section 3.3). The transverse sample was cut perpendicularly to the running direction. The Keyence VHX-5000 light optical microscopy (LOM) was employed to first inspect the surface damage before sample preparation, and then investigate plastic deformation along the depth of rail head in the longitudinal and transverse directions in the rail samples. The two types of samples provide a comprehensive observation of plastic deformation of the rail head material, which is critical for the in-depth investigation of HC damage.

3. Results

3.1. Wheel–rail contact loads

Fig. 5 shows the wheel–rail contact loads measured on the V-Track above sleepers No. 71–73 (R260MN steel) at different load cycles. The longitudinal and vertical loads and the resultant traction coefficients demonstrate good repeatability. There are some variations in the lateral forces. That can be resulted from the changes of wheel profile in the transverse direction, including the conicity, due to wear and plastic deformation under the cyclic loading.

3.2. Contact analysis using BEM

The measured wheel–rail contact forces and the geometric spin were then used as inputs for the CONTACT program to calculate the elastic contact solutions on the rail above the sleeper NO. 72. The steel grade at this location of interest is R260MN. The calculated elastic contact stress states inside the running band are shown in Fig. 6. Due to the presence of geometrical spin [5,30],

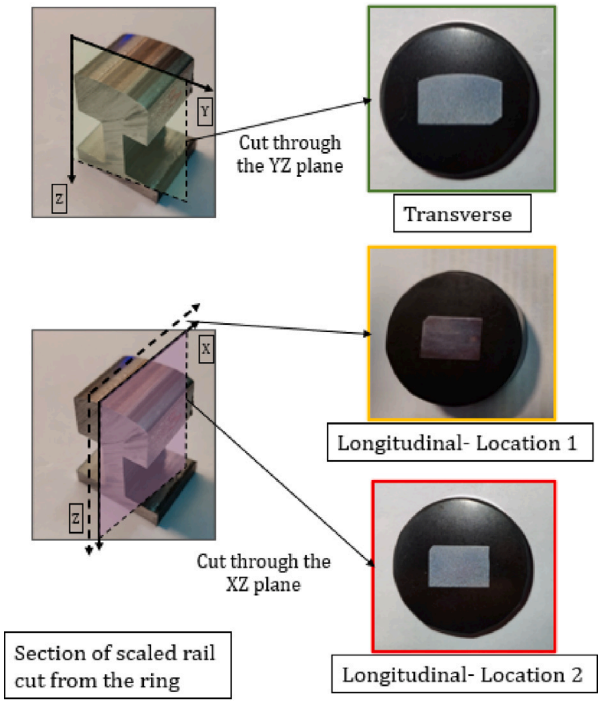

Fig. 4. Overview of the selection of the transverse and longitudinal samples.

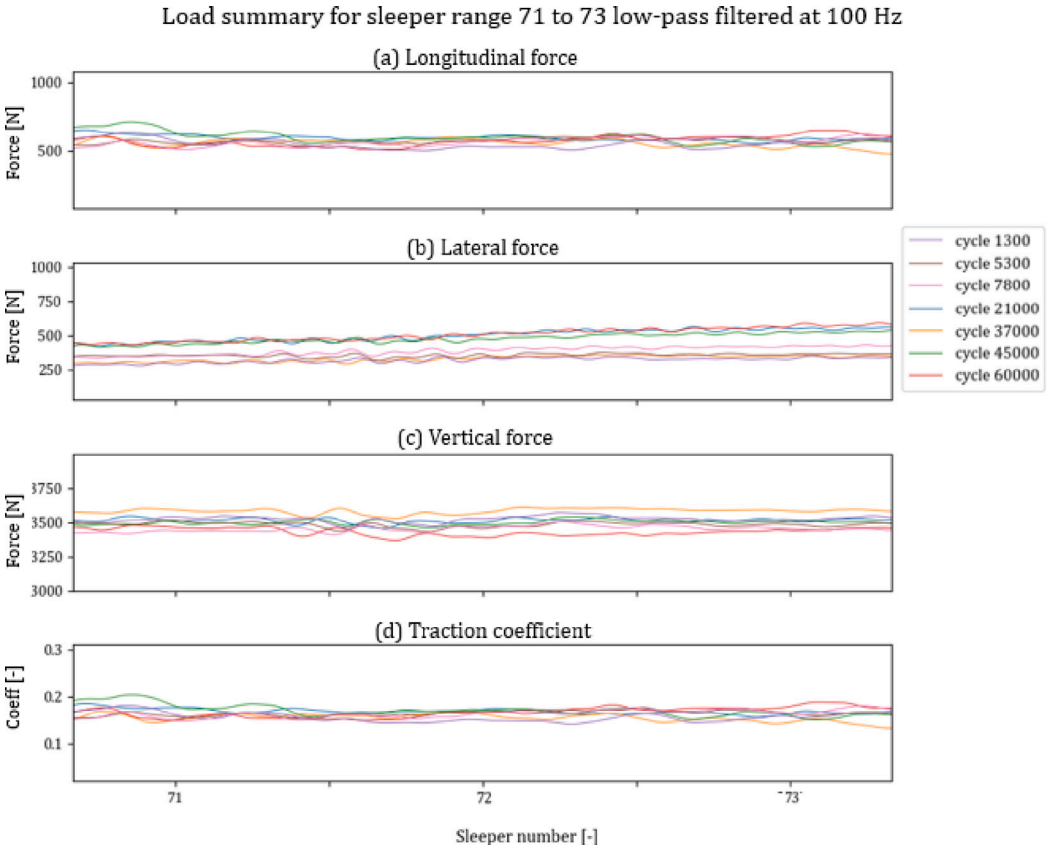

Fig. 5. Overview of the loads measured from V-Track at different cycles: (a) longitudinal force (b) lateral force (c) vertical force (d) the traction coefficient.

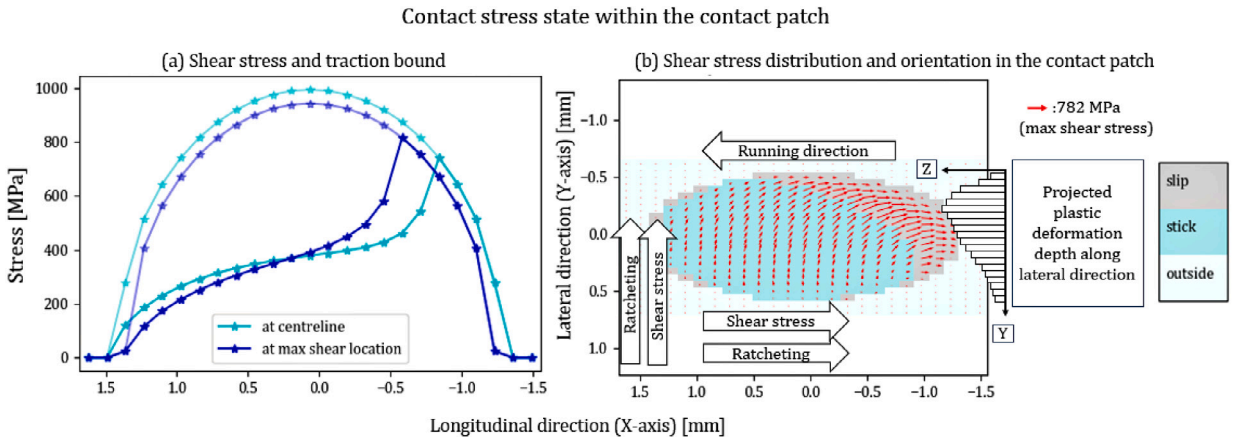

Fig. 6. Contact analysis results and predictions of ratcheting: (a) shear stress magnitude in the contact patch determined by CONTACT, and (b) distribution and orientation of the shear stress within the contact patch and ratcheting patterns predicted based on the shear stress.

the orientation of the surface shear stress exhibits a rotational pattern, as indicated in Fig. 6(b). In addition, because a positive torque was applied to the wheel to simulate a traction loading case, the longitudinal components of the surface shear stress orientate to the opposite direction of the running direction of the wheel.

Although the elastic contact stress state cannot be used to accurately predict plastic deformation and ratcheting, it can provide valuable insights into a potential ratcheting pattern within the running band, as depicted in Fig. 6(b). The ratcheting, as a consequence of contact-induced plastic flow, is expected to be produced following the directions of contact shear stresses, because the contact shear stresses are the key components in the deviatoric stresses [33,34] that governs the plastic flow in wheel–rail contact [9]. Notably, as the longitudinal component of the shears stress is opposite to the running direction of the wheel, ratcheting indicated by the accumulated plastic shear strain [12], is expected to orientate against the wheel running direction(along the positive X-axis). The plastic shear strain in the lateral direction is anticipated to orient to the right when observing along the running direction. In addition, a layer of plastic deformation identifiable via the shear strains, can be expected to accumulate more in the depth of the rail (on the Z-axis), on the right side of the running band, where the shear stress magnitudes are higher indicated by the length of the arrows in Fig. 6(b). Thus according to the magnitudes of the shear stresses, the projected depth of the plastic deformation accumulated along the lateral direction (Y-axis) is depicted on the right in Fig. 6(b). The corresponding experimental results of the ratcheting and plastic deformation will be presented in Section 3.4 through a microscopic analysis.

3.3. Rail surface observation

A visual inspection was conducted to identify the possible damage on the rail surface and to decide the locations to cut rail samples for the subsequent microscopic analysis. Surface damage was found to emerge in the form of cracks and visible irregularities after about 10,000 load cycles. Upon termination of the test at 60,000 cycles, significant surface damage was observed on the R260MN rail, as shown in Fig. 7. Zooming in on the surface damage under LOM (Fig. 7(b), we can observe two distinctive zones with the surface damage: Zone 1, within the yellow rectangle frame in Fig. 7, exhibited notable surface irregularities; and Zone 2, within the red rectangle frame, can be identified as a flatter and more reflective surface than that in Zone 1, with much less visible roughness, possibly worn during rolling contact [35,36]. Cracks were observed in both zones. The microscopic analysis presented in the next section focused on two longitudinal samples respectively at these two zones in the ZX plane and a transverse sample covering both zones in YZ plane per Fig. 4.

3.4. Microscopic analysis

The plastic flow observed from a longitudinal rail sample cut at the centreline of Zone 1 is shown in Fig. 8. It can be seen that the plastic flow direction aligns with the wheel running direction. This contradicts the elastic wheel–rail contact solutions presented in Section 3.2 predicting that ratcheting opposes the wheel running direction. The reason is that Zone 1 is out of the rail running band (i.e. no wheel–rail contact occurs here), to be explained later. In the plastically deformed layer that is shallower than 150 μm visible by the deformed lamellae as shown in Fig. 8(b), surface cracks were visible and developed along the direction of plastic flow.

In contrast to the results observed in Zone 1, the sample from Zone 2 exhibited plastic flow opposite to the running direction, as depicted in Fig. 9. This observation aligns with the ratcheting direction predicted based on wheel–rail contact solutions presented in Section 3.2. Cracks can be observed to develop also opposite to the running direction between the plastically deformed lamellae. The plastically deformed layer in Zone 2 is about 300 μm, deeper than that in Zone 1 (c.a. 130 μm), indicating that Zone 2 experienced a more severe plastic deformation due to higher shear stresses.

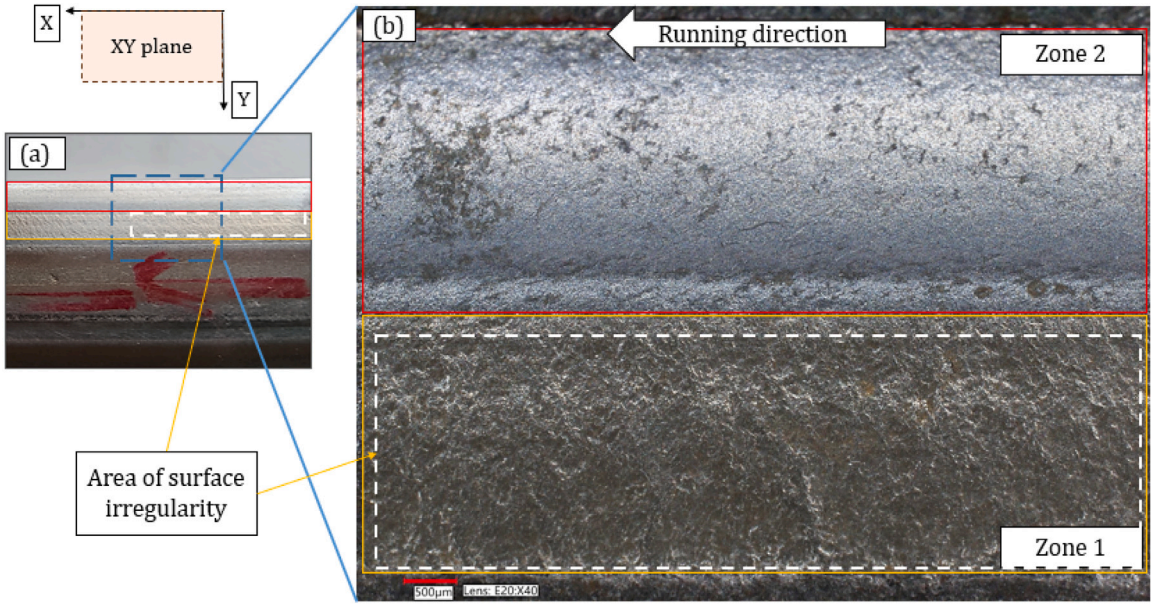

Fig. 7. Identified Zone 1 and Zone 2 from the surface observation, (a) the observed surface damage (b) the microscopic view of the surface damage to identify the Zone 1 and Zone 2.

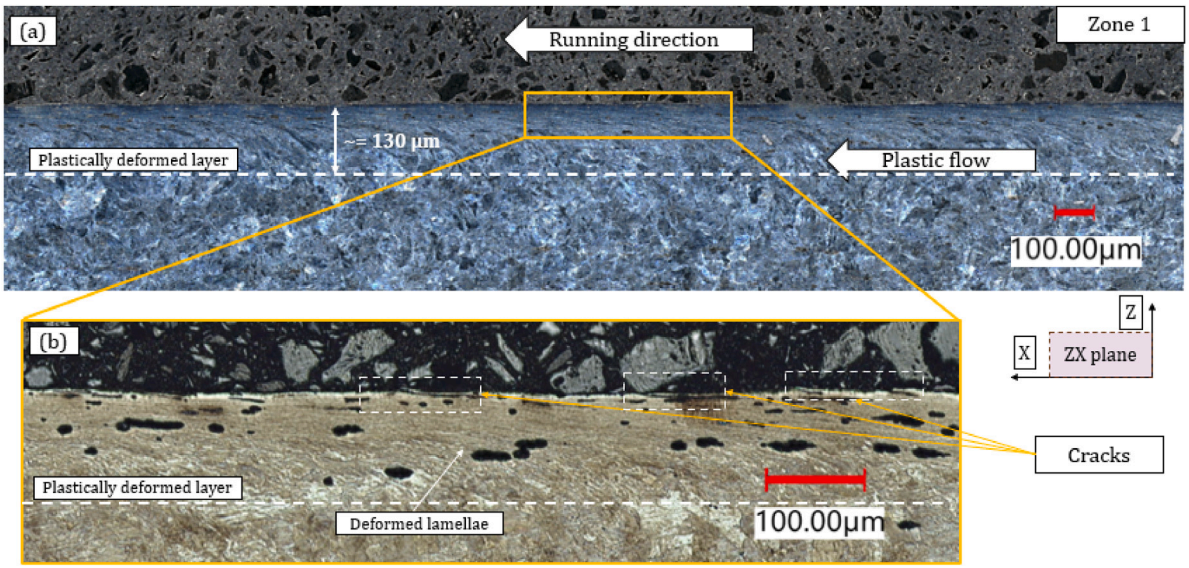

Fig. 8. The microscopic analysis results in Zone 1 (a) an over view of the plastic deformation in Zone 1 (b) ta close-up view of the cracks in Zone 1.

The microscopic results of the transverse sample in Zone 2 per Fig. 10 demonstrate strong correlation with the contact solutions presented in Section 3.2. As shown in Fig. 10(a), deeper plastic deformation was observed on the right side of the running band, following the running direction. This corresponds to the high shear stress region shown in Fig. 6. The ratcheting exhibited the same orientation as the lateral component of the shear stress in the contact patch. Cracks were also visible and followed the direction of plastic deformation in the transverse sample. The layer of plastic deformation, whose region is distinguished in Fig. 10(a) by a green dashed curve, in Zone 1 appeared shallower than that in Zone 2 (same as observed in the longitudinal samples), and looked like a 'tail' or an extension of plastic deformation in Zone 2. In addition, the analysis of the lateral sample also indicates that the plastic flow in Zone 1 exhibited a direction opposite to that in Zone 2, which is in line with the findings obtained from the longitudinal sample cuts.

The microscopic analysis results show that in Zone 2, the plastic flow orientation agrees well with the shear stress pattern obtained with BEM presented in Fig. 6. This demonstrates that the orientations of the shear stresses within the contact patch

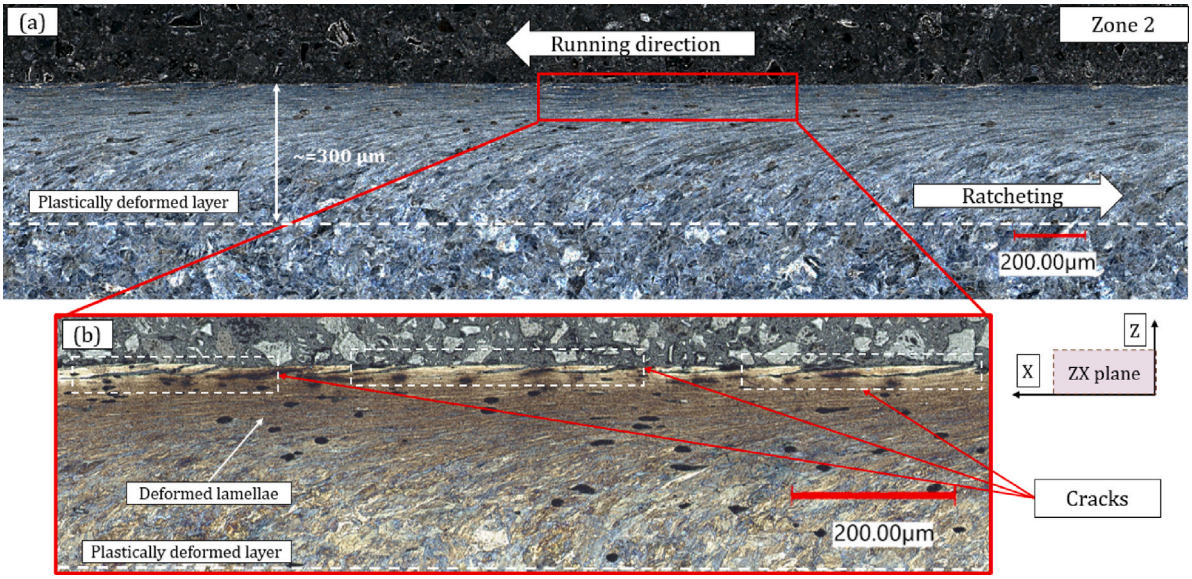

Fig. 9. The microscopic analysis results in Zone 2 (a) an overview of the plastic deformation in Zone 2 (b) a close-up view of the cracks in Zone 2.

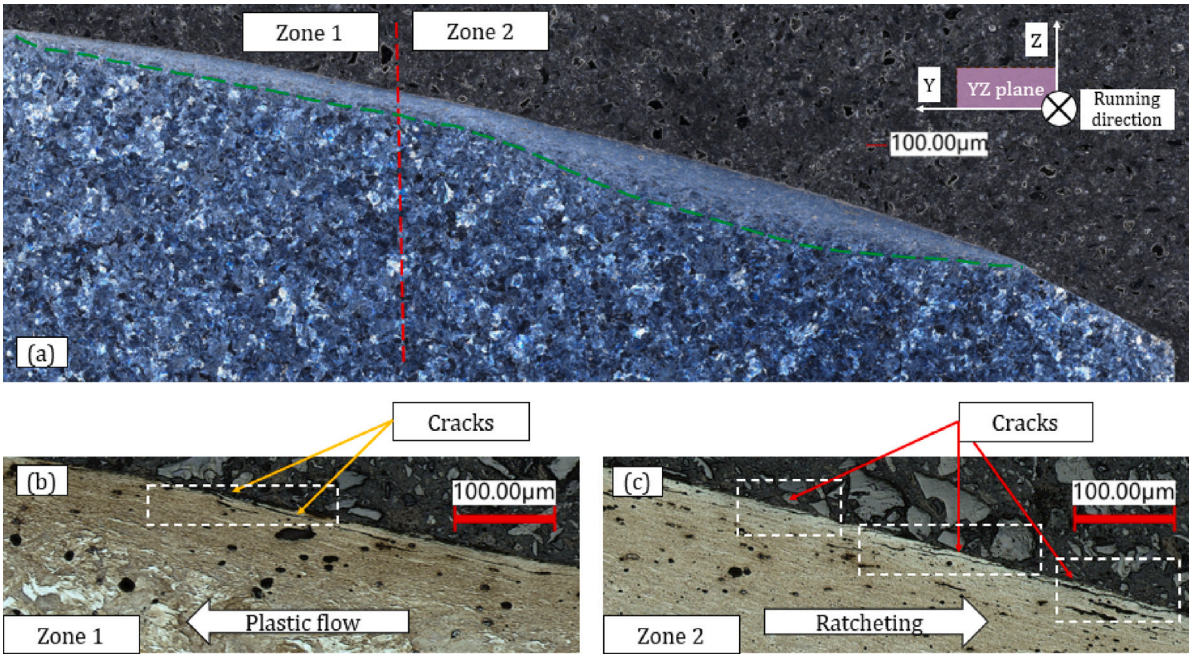

Fig. 10. The microscopic analysis results from the transverse sample (a) an overview of the range of the plastic deformation in both Zone 1 and Zone 2 (b) a close-up view of Zone 1 with cracks and plastic flow (c) a close-up view of Zone 2 with cracks and ratcheting.

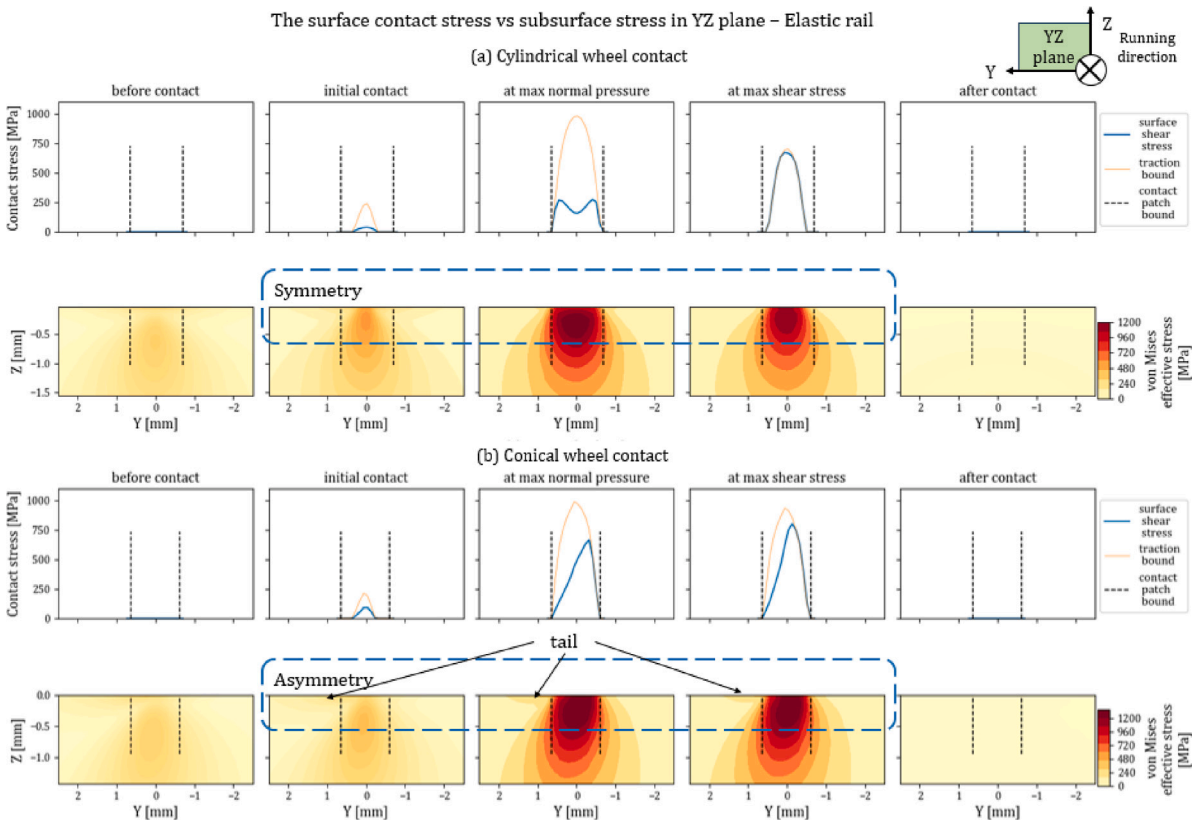

Fig. 11. Comparison of the surface contact shear stress and subsurface von-Mises stress between cylindrical and conical wheel contacts based on elastic rail material (a) the cylindrical wheel contact — without geometrical spin (b) conical wheel contact — with geometrical spin.

determine the directions of plastic flow or ratcheting generated in the running band. The cracks observed in this zone are then expected to develop into HC cracks. In Zone 1, however, the plastic flow shows an opposite trend, which was not in line with the contact analysis. One possible reason is that Zone 1 was outside the running band, and the plastic deformation in Zone 1 was generated mainly by subsurface stresses, instead of surface contact stress, under the wheel–rail rolling contact. A further analysis using the FE method was conducted to examine this phenomenon, and the results are presented in the next section.

3.5. FEM analysis

Fig. 11 compares the surface contact shear stress and subsurface von-Mises stresses of the elastic rail in contact with the cylindrical (Fig. 11(a) and conical wheels (Fig. 11(b). The YZ cross-section stresses are presented in five phases of a wheel–rail rolling contact cycle in the simulation (from left to right in Fig. 11): before contact, at the initial contact, at the location of the maximum normal contact pressure and thus traction bound, at the location of the maximum surface shear stress, and after contact. By comparing the surface shear stresses and traction bounds solved by the FE conical contact model (the 3rd and 4th phases in Fig. 11(b) to CONTACT solutions (see, Fig. 6), they align well with each other in terms of amplitudes and patterns, demonstrating the accuracy of the FE model.

For the cylindrical wheel case, symmetrical patterns of stress distributions were observed on the surface and in the subsurface, since there was no influence of the geometrical spin. With the conical wheel contact, however, the asymmetry in the surface contact shear stress due to geometrical spin caused the asymmetric reactions of subsurface stresses as well. In Fig. 11(b), we can see a ‘tail’ in the subsurface von-Mises stress outside and to the left of the contact patch during the contact (the 2nd, 3rd and 4th phases), with the running direction pointing into the paper. Notably, the location of the tail found in the FE simulation corresponds well to the location of Zone 1 observed in the microscopic analysis, as shown in Fig. 10. The magnitude of von-Mises stresses in this ‘tail’ is significantly lower than that within the contact patch, indicating a weaker effect to yield the rail material. This also corresponds to the shallower plastic deformation observed in Zone 1 in Fig. 10.

Considering that the ultimate strengths of pearlitic rail steels are rarely above 1200 MPa [37,38], the consideration of rail plasticity is necessary to represent a more ‘realistic’ situation. The von-Mises stresses obtained from the simulations of BLKH rails in contact with the cylindrical and conical wheels are presented in Fig. 12. Compared to elastic FE contact results presented in Fig. 11, the peak von-Mises stresses were significantly lower when the BLKH rail was used. Fig. 12(b) shows a similar left ‘tail’ for the case

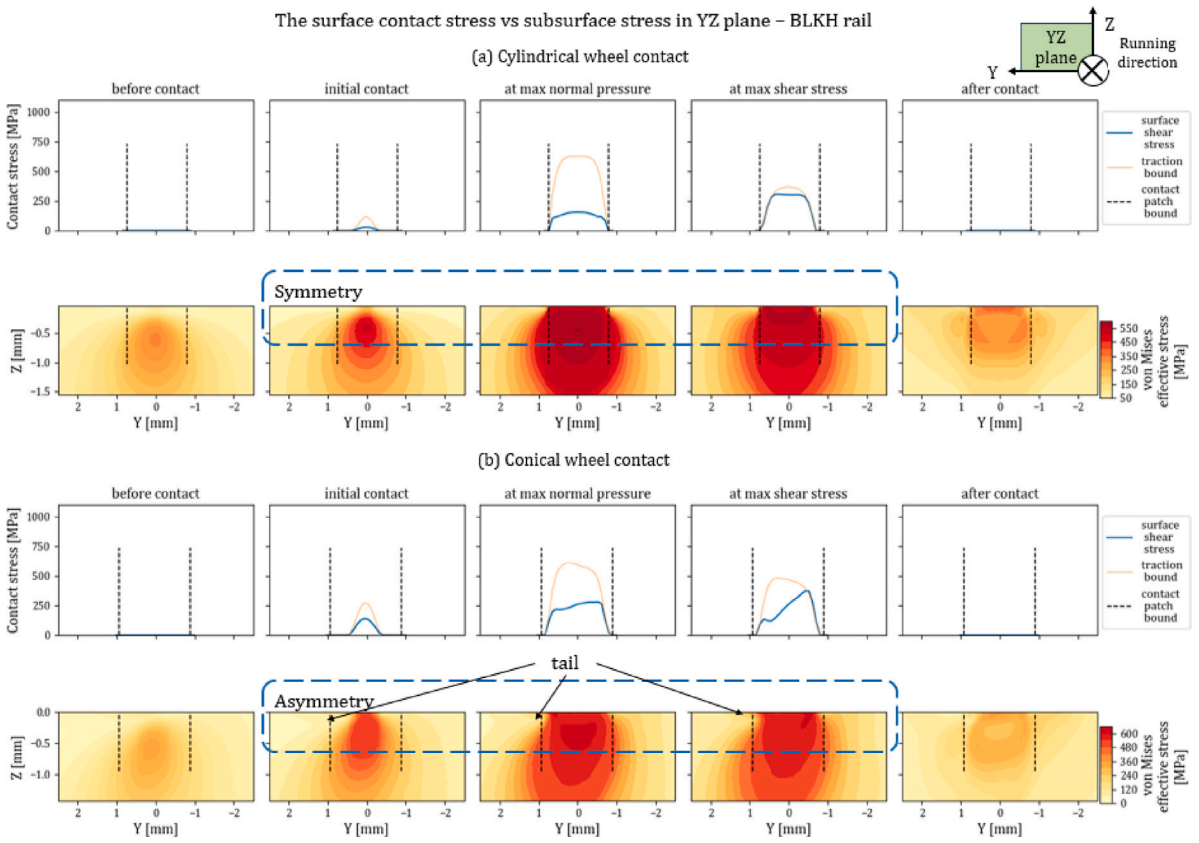

Fig. 12. Comparison of the surface contact shear stress and subsurface von-Mises stress between cylindrical and conical wheel contacts based on BLKH rail material (a) the cylindrical wheel contact — without geometrical spin (b) conical wheel contact — with geometrical spin.

of the conical wheel–rail contact (the 2nd, 3rd and 4th phases). Another difference lies in the stress states after the contact (the 5th phase), where we can see residual stress in the subsurface region in Fig. 12. The difference in the distribution symmetry between the contacts with the cylindrical and conical wheels was also present for the residual von-Mises stresses.

To further investigate the changes in stresses over one contact cycle, the normal and shear stresses of the surface elements were presented in the XY plane in Fig. 13. The stresses within the contact patch boundary in Fig. 13, are directly induced by the surface contact stresses, whereas those outside are considered as the secondary effect as the rail responds to the rolling contact. The stresses were compared between the cylindrical and conical wheel contact cases. The cylindrical contact results (the left column) exhibited symmetric patterns with respect to the longitudinal central line, whereas asymmetry in the stress distribution was observed in the conical contact case (the right column). As shown in Fig. 13(a), (b) and (c), the wheel–rail contact-induced compressive stress within the contact patch is much higher than that beyond. The normal stresses are predominantly compression in the X, Y, and Z directions within the contact patch indicated by the negative values; and those with positive values suggest tensile stresses outside, especially adjacent to the running band for the cylindrical contact and to the left boundary of the running band for the conical contact case. The latter corresponds well to the location of Zone 1 observed in the microscopic analysis shown in Fig. 8(a).

Furthermore, the 3 compressive normal stress components (σ_{11}, σ_{22}, σ_{33}) within the contact patch are quite close to one another in magnitude, resulting in a relatively high hydrostatic stress, σ_p, [33], as shown in Eq. (2):

$$\boldsymbol{\sigma} = [\sigma_{ij}] = \begin{bmatrix} \sigma_{11} & \sigma_{12} & \sigma_{13} \\ \sigma_{21} & \sigma_{22} & \sigma_{23} \\ \sigma_{31} & \sigma_{32} & \sigma_{33} \end{bmatrix} \tag{1}$$

$$\sigma_p = \frac{1}{3} Tr(\boldsymbol{\sigma}) = \frac{1}{3}(\sigma_{11} + \sigma_{22} + \sigma_{33}) \tag{2}$$

Where $\boldsymbol{\sigma}$ is the stress tensor, $Tr(\cdot)$ is the trace of the tensor. This high hydrostatic stress diminishes the contribution of the normal stresses to the deviatoric stresses, s_{ij}, as demonstrated in Eq. (3), and consequently yield of the material according to von-Mises J2 criterion [33,34] in Eq. (4) and (5):

$$s_{ij} = \sigma_{ij} - \sigma_p \delta_{ij} \tag{3}$$

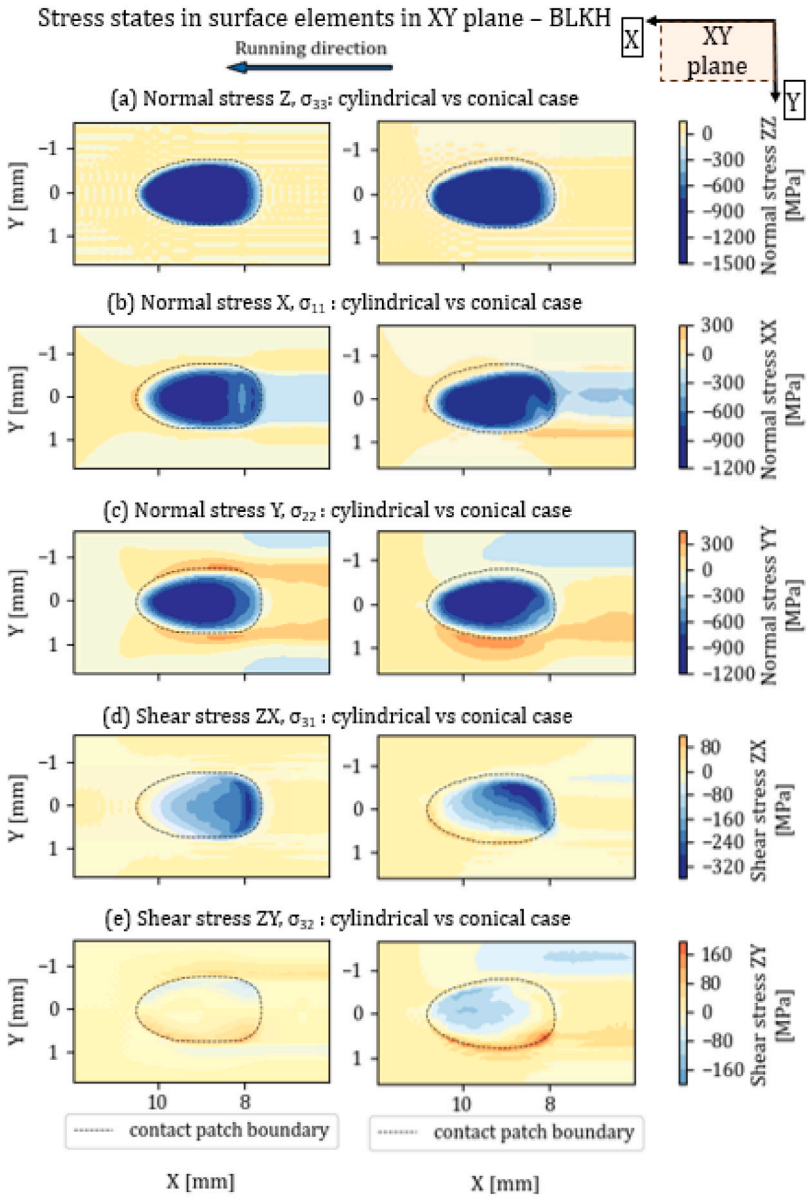

Fig. 13. Stress states in the XY plane of the rail elements close to surface induced by the cylindrical and conical wheels : (a) normal stress in Z, (b) normal stress in the X direction (c) normal stress in Y (d) shear stress along X perpendicular to Z, and e) shear stress along Y perpendicular to Z.

$$f = \frac{3}{2} s_{ij} s_{ij} - \sigma_y^2 \tag{4}$$

$$\sigma_{vm} = \sqrt{\frac{3}{2} s_{ij} s_{ij}} = \sqrt{\frac{3}{2}[s_{11}^2 + s_{22}^2 + s_{33}^2 + 2(s_{31}^2 + s_{32}^2 + s_{12}^2)]} \tag{5}$$

Where the Kronecker delta $\delta_{ij} = 1$ if $i = j$, or 0 if $i \neq j$. Therefore, within the contact patch, shear stresses exert the most significant influence among the deviatoric stresses that decide the plastic flow or ratcheting. This can be further explained by the normality flow rule of constitutive plasticity theory [9,34,39], as shown in Eq. (6):

$$d\epsilon_{ij}^p = \frac{3}{2} \frac{1}{h} \langle n_{ij} d\sigma_{ij} \rangle n_{ij} \tag{6}$$

$$n_{ij} = \frac{\frac{\partial f}{\partial \sigma_{ij}}}{\sqrt{\frac{\partial f}{\partial \sigma_{kl}} \frac{\partial f}{\partial \sigma_{kl}}}}, \frac{\partial f}{\partial \sigma_{ij}} = \frac{\partial f}{\partial s_{ij}} \tag{7}$$

$$= \frac{s_{ij}}{\sqrt{s_{kl} s_{kl}}} \tag{8}$$

Where $d\epsilon_{ij}^p$ is the incremental plastic strain tensor, h is the scalar plastic modulus, and n_{ij} is the unit tensor of the gradient of the yield surface with respect to stress, $\partial f / \partial \sigma_{ij}$, as specified in Eq. (7). The Macaulay bracket $\langle \cdot \rangle$ returns 0 if the scalar $n_{ij} d\sigma_{ij}$ is negative, and therefore stipulates that plastic flow occurs only when the change in stresses aligns with the gradient of the yield function, f. Eq. (6) and (8) indicate that the deviatoric stress tensor is directly linked to the increment plastic strain tensor.

According to the plasticity theory explained above, the stress states determined from the FEM thus support our findings in Section 2.3 that the ratcheting and shear stress within the running band are highly correlated. In contrast, outside the contact patch, the (residual) tensile stress in the Y direction, σ_{22}, is higher in magnitude than those in the X and Z directions (σ_{11}, σ_{33}), with the latter being negligible. This disparity in the normal stresses outside the contact patch leads to a low hydrostatic stress (Eq. (2)), and thus elevates the weight of the X and Y normal stresses in the deviatoric stress (Eq. (2)) and von-Mises stress (Eq. (5)), whereas the influence of the shear stresses is less pronounced compared with those inside the contact patch as shown in Fig. 13.

The asymmetry in the shear stresses displayed in Figs. 13(d) and 13(e) shows that higher shear stresses took place to the right of the running direction. Furthermore, the lateral friction force resulting from the wheel conicity created higher lateral shear stresses in the contact patch than that in the cylindrical contact case. For both shear stresses in the conical contact case, components in the positive X and Y axes were present close to the left boundary of the running band, again aligning with the direction of plastic deformation in Zone 1 observed in the microscopic analysis, as shown in Figs. 8 and 10(b).

Although the normal and shear stresses outside the contact patch are not as high as that within the contact patch for a single load cycle, the residual normal stresses may accumulate with increasing load cycles, especially in view that during cyclic loading, plastic deformation may accumulate in the running band, changing the contact geometry, so that the stresses outside the contact patch may increase and plastic deformation may accumulate there, too. Given the substantial normal stresses occurring outside the running band over one contact cycle, the yield of the material in Zone 1 can be caused by the deviatoric components from the accumulated normal stresses combined with the shear stresses. This could explain the smaller shear strain (smaller inclination of the lamellae) and the shallower plastic deformation layer in Zone 1 compared to Zone 2 as depicted in Figs. 8, 9, and 10(b). It is thus of interest to investigate the effects of the cyclic rolling contacts in further studies.

3.6. Correlation analysis of contact stress-plastic strain

The contact-induced stress states on the rail surface simulated using the BLKH material are depicted in Fig. 14. A comparison of Figs. 14(a) and (b) confirms that the orientations of the shear stresses within the surface elements, represented by tensor components σ_{31} and σ_{32} (perpendicular to the Z-axis, along the X and Y-axes respectively), generally align well with the surface contact shear stresses, particularly within the central region of the contact patch. The differences in the amplitudes of these two types of shear stresses arise from the fact that the shear stress tensors are determined at the central integration points of the surface elements, whereas the contact shear stresses are derived directly from the surface nodal forces, in addition to the presence of the components, σ_{12} (XY) within the surface elements. Fig. 14(b) illustrates distinct patterns in the shear stress orientation within the surface elements at and beyond the edges of the contact patch, which differ from the surface contact shear stress distribution. This difference can be attributed to the secondary effects of rolling contact, as discussed in Section 3.5. Specifically, at location 2-3 of Zone 2, positioned adjacent to Zone 1, minimal σ_{31} and σ_{32} components are observed, indicating asymmetry in the shear stress distribution for the conical wheel contact, as elaborated in Section 3.5. This asymmetry is further evident in Fig. 14(c), where the maximum normal and shear contact stresses are compared to the von Mises effective stress along the lateral direction of the rail.

To examine possible correlation between the stresses and plastic strains, three locations within Zone 2 and one location with a high effective stress in Zone 1, as denoted by '2-1', '2-2', '2-3' and '1-1' in Fig. 14(b), were selected, and their corresponding stress values are presented in Table 1. The deviatoric stresses, s_{ij} (see Eq. (3)), are used in the following discussion. At location 2-1, the maximum effective stress within the contact patch reached 626.97 MPa, exceeding the yield stress of 500 MPa, as illustrated in Fig. 14(c). One of the highest values s_{31} (ZX) is present at this location, contributing significantly to the effective stress ($\sqrt{3/2 * 2 * 335.94^2} = 581.86$ MPa), according to Eq. (5), while the values of s_{ii} remain less significant due to the high hydrostatic stress (σ_p of −935.93 MPa). The negative value of s_{31} indicates that plastic flow is oriented opposite to the running direction (-X), which can be correlated with the ratcheting orientation observed in Zone 2, as shown in Fig. 9.

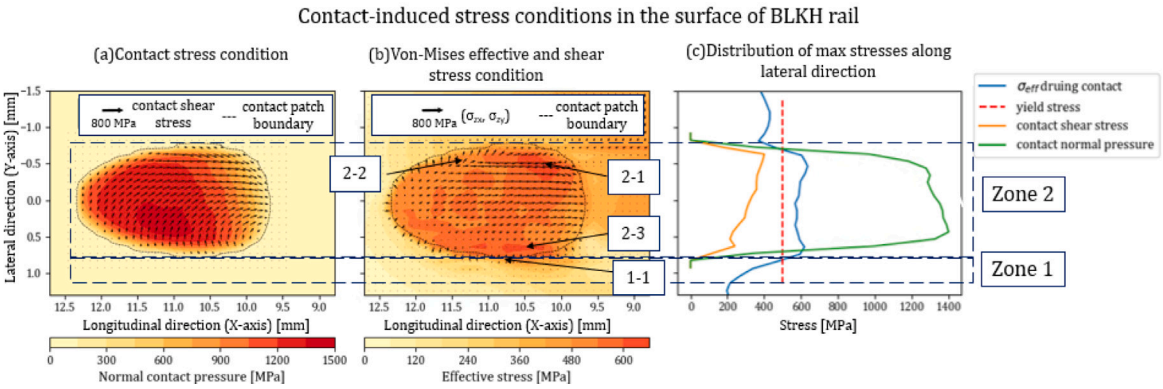

Fig. 14. Contract-induced stress conditions in Zones 1 and 2: (a) surface contact stress conditions simulated with the BLKH rail, (b) effective stress conditions in the surface elements during contact, and (c) distribution of maximum normal contact pressure, shear stress and effective stress in surface elements.

Table 1
Deviatoric, hydrostatic, and effective stresses and correlation with plastic strain in Zones 1 and 2.

Locations	s_{11}	s_{22}	s_{33}	s_{31}	s_{32}	s_{12}	σ_p	σ_{eff}	Plastic flow direction	Plastic shear strain depth
Zone 1 1–1	−85.81	241.46	−155.66	20.83	52.23	−160.68	120.83	470.94	+X, +Y	~130
Zone 2 2–1	−98.70	102.15	−3.45	−335.94	50.87	−74.12	−935.93	626.97	-X, +Y	~300
Zone 2 2–2	190.41	−26.66	−163.75	1.67	−234.90	−19.62	−594.69	512.22	+X, -Y	~300
Zone 2 2–3	77.42	310.75	−388.17	−20.19	6.92	21.15	−1046.38	618.52	-X, +Y	~130

*Deviatoric stresses are determined according to Eq. (3)
** All stresses are in MPa.
*** The plastic shear strain depth is measured in μm. The values were estimated from Fig. 10 for indication only.

Additionally, there is a small but positive value of s_{32} (50.78 MPa) at location 2-1. However, it is important to consider location 2-2 because the stress condition at location 2-1 will subsequently occur at location 2-2 as the wheel rolls forward. Location 2-2 exhibits an effective stress of 512.22 MPa, which also exceeds the yield strength. A high value of s_{32} (−234.9 MPa) at this location indicates plastic flow in the negative lateral direction, corresponding well with the orientation of the accumulated shear strain in Zone 2, as shown in Fig. 10(c). Furthermore, the highest effective stresses together with highest shear stress levels at these locations, correlate with the largest plastic deformation as indicated by the accumulated plastic shear strains and observed in our microscopic analysis shown in Fig. 9.

Location 2-3 represents a special case within the contact patch where a relatively high effective stress is reached (Fig. 14(c)) despite relatively low shear stresses (Figs. 14(b)). As indicated in Table 1, both s_{22} and s_{33} contribute significantly to the effective stress, calculated as $\sqrt{3/2 * (310.75^2 + 388.17^2)} = 608.98$ MPa. This is attributed to the highest normal contact pressure occurring near the bottom edge of the contact patch, as shown in Fig. 14(c), where the secondary contact effects significantly reduce both the compressive σ_{11} (X) and σ_{22} (Y), as illustrated in Fig. 13(b) and (c). Despite the high effective stresses, a small negative s_{31} and a minimal positive s_{32} are present at location 2-3, contributing to a plastic flow opposite to the running direction but moderately accumulated plastic shear strain visible along the depth of rail, as observed near Zone 1 in Fig. 10.

The stresses σ_{11} and σ_{22} transition to tensile states outside the contact patch, with their deviatoric stress values for Zone 1 provided in Table 1. Similar to location 2-3, the normal deviatoric stresses, s_{22} and s_{33} contribute significantly to the effective stress, along with s_{12}, as discussed in Section 3.5. As indicated in Fig. 14 and Table 1, yielding of the rail does not occur in Zone 1 during the first rolling contact cycle. Nonetheless, small positive values of s_{31} and s_{32} are present, which correspond to a potential plastic flow in the wheel running direction (+X) and in the positive Y direction. This observation correlates well with the plastic deformation observed in Zone 1, as depicted in Figs. 8 and 10(a) and (b).

In summary, the contact shear stress serves as an indicator of the shear stress conditions within surface elements, especially in the central part of the contact patch (Zone 2), while the orientation and amplitude of these shear stresses are affected by secondary effects arising from contacts adjacent to and beyond the contact patch edges (Zone 1). These secondary effects can also result in material yielding at the edge of the contact patch without significant shear stress.

4. Conclusion and further study

This study demonstrated the capability of the V-Track test rig to generate RCF-induced damage in the rail surface under controlled contact conditions. The measured wheel–rail contact forces showed good repeatability, ensuring consistent loading conditions for a large number of load cycles. The contact shear stress under the same loading condition was calculated using BEM to predict the

orientation of plastic flow within the running band. Subsequently, a microscopic analysis confirms the strong correlation between the contact shear stress and ratcheting patterns in both the longitudinal and lateral directions. The decisive role of contact shear stress in ratcheting formation was further supported by the FEM analysis. Moreover, the microscopic analysis shows an opposite pattern of plastic flow outside the contact patch. The phenomenon was further investigated and explained via FE wheel–rail contact simulations incorporating plasticity in the rail material. The asymmetry distribution of the subsurface stress states during the conical wheel contact gives rise to significant normal and shear stresses beyond the running band. The directions of the stresses are opposite to those within the running band. This distribution of the normal and shear stresses indicates the possibility of material yield and plastic flow opposite to the ratcheting orientation within the running band when their residuals accumulate with the wheel–rail load cycles.

The application of the BLKH material model has demonstrated a more reasonable contact stress states for the wheel–rail contact compared to the elastic material model. The stress states determined with the FE simulations, especially using the BLKH material model, shed lights on the possible cause of the plastic flow outside the running band observed from the HC test. Nonetheless, the BLKH material model cannot simulate the ratcheting effects [34] and therefore not ideal for simulating the accumulation of plastic deformation under cyclic rolling contacts. To address this limitation, the non-linear kinematic hardening (NLKH) material should be used instead for accurate simulations to study RCF initiation [1,34]. Therefore, the next step of this study involves calibrating the rail steels used in the V-Track HC tests with constitutive material models capable of representing the NLKH behaviour of the material [34,40]. Furthermore, the simulations of RCF should incorporate cyclic loading [32,41–43] and induced wear evolution [44,45], enabling the simulations of residual stress accumulation, the change of the contact profile and stresses, and further investigation into the crack initiation mechanism within and beyond the running band.

CRediT authorship contribution statement

Fang Ren: Writing – original draft. **Zhen Yang:** Writing – review & editing. **Zili Li:** Writing – review & editing.

Declaration of competing interest

There is no conflict of interest.

Acknowledgements

This study is part of the Maximise the rail Life (MaxLife) research project, conducted at Delft University of Technology. The MaxLife project (code: 15796), is funded by the Dutch Research Council (NWO) and Dutch rail infrastructure manager, ProRail.

Data availability

Data will be made available on request.

References

[1] A.F. Bower, The influence of crack face friction and trapped fluid on surface initiated rolling contact fatigue cracks, J. Tribol. 110 (4) (1988) 704–711, http://dx.doi.org/10.1115/1.3261717.
[2] D. Fletcher, F. Franklin, A. Kapoor, Rail surface fatigue and wear, in: R. Lewis, U. Olofsson (Eds.), Wheel–Rail Interface Handbook, Elsevier, 2009, pp. 280–310, http://dx.doi.org/10.1533/9781845696788.1.280.
[3] R. Heyder, M. Brehmer, Empirical studies of head check propagation on the DB network, Wear 314 (1–2) (2014) 36–43, http://dx.doi.org/10.1016/j.wear.2013.11.035.
[4] S.L. Grassie, Rolling contact fatigue on the british railway system: treatment, Wear 258 (7–8) (2005) 1310–1318, http://dx.doi.org/10.1016/j.wear.2004.03.065.
[5] R. Dollevoet, Z. Li, O. Arias-Cuevas, A method for the prediction of head checking initiation location and orientation under operational loading conditions, Proc. Inst. Mech. Eng. F J. Rail Rapid Transit 224 (5) (2010) 369–374, http://dx.doi.org/10.1243/09544097jrrt368.
[6] R. Stock, R. Pippan, RCF and wear in theory and practice—The influence of rail grade on wear and RCF, Wear 271 (1–2) (2011) 125–133, http://dx.doi.org/10.1016/j.wear.2010.10.015.
[7] Y. Zhou, S. Wang, T. Wang, Y. Xu, Z. Li, Field and laboratory investigation of the relationship between rail head check and wear in a heavy-haul railway, Wear 315 (1–2) (2014) 68–77, http://dx.doi.org/10.1016/j.wear.2014.04.004.
[8] S.K. Paul, A critical review of experimental aspects in ratcheting fatigue: microstructure to specimen to component, J. Mater. Res. Technol. 8 (5) (2019) 4894–4914, http://dx.doi.org/10.1016/j.jmrt.2019.06.014, URL https://www.sciencedirect.com/science/article/pii/S2238785419300900.
[9] A. Bower, K. Johnson, The influence of strain hardening on cumulative plastic deformation in rolling and sliding line contact, J. Mech. Phys. Solids 37 (4) (1989) 471–493, http://dx.doi.org/10.1016/0022-5096(89)90025-2.
[10] A. Kapoor, Wear by plastic ratchetting, Wear 212 (1) (1997) 119–130, http://dx.doi.org/10.1016/s0043-1648(97)00083-5.
[11] G. Donzella, M. Faccoli, A. Mazzù, C. Petrogalli, R. Roberti, Progressive damage assessment in the near-surface layer of railway wheel-rail couple under cyclic contact, Wear 271 (1–2) (2011) 408–416, http://dx.doi.org/10.1016/j.wear.2010.10.042.
[12] W.R. Tyfour, J.H. Beynon, A. Kapoor, Deterioration of rolling contact fatigue life of pearlitic rail steel due to dry-wet rolling-sliding line contact, Wear 197 (1–2) (1996) 255–265, http://dx.doi.org/10.1016/0043-1648(96)06978-5.
[13] D. Fletcher, S. Lewis, Creep curve measurement to support wear and adhesion modelling, using a continuously variable creep twin disc machine, Wear 298–299 (2013) 57–65, http://dx.doi.org/10.1016/j.wear.2012.11.065.

[14] X. Zhao, Q. Chen, Y. Liu, X. Qiu, E. Meli, A. Rindi, Effects of slip ratio and contact stress on rolling contact fatigue of defected rail materials, Eng. Fail. Anal. 131 (2022) 105817, http://dx.doi.org/10.1016/j.engfailanal.2021.105817.
[15] Y. Li, Y. Wu, P. Mutton, C. Qiu, W. Yan, A ratcheting mechanism-based numerical model to predict damage initiation in twin-disc tests of premium rail steels, Eng. Fail. Anal. 146 (2023) 107066, http://dx.doi.org/10.1016/j.engfailanal.2023.107066.
[16] D. Chen, M. Zhong, M. Mou, Q. Xiao, X. Liu, W. Yang, S. Zhu, B. Liu, F. Lin, X. Shi, Research on the damage mechanism of the rolling contact fatigue of a wheel–rail contact system under the influences of surface defects, Eng. Fail. Anal. 164 (2024) 108631, http://dx.doi.org/10.1016/j.engfailanal.2024.108631.
[17] A. Monk-Steel, D. Thompson, F. de Beer, M. Janssens, An investigation into the influence of longitudinal creepage on railway squeal noise due to lateral creepage, J. Sound Vib. 293 (3–5) (2006) 766–776, http://dx.doi.org/10.1016/j.jsv.2005.12.004.
[18] D.T. Eadie, D. Elvidge, K. Oldknow, R. Stock, P. Pointner, J. Kalousek, P. Klauser, The effects of top of rail friction modifier on wear and rolling contact fatigue: Full-scale rail-wheel test rig evaluation, analysis and modelling, Wear 265 (9–10) (2008) 1222–1230, http://dx.doi.org/10.1016/j.wear.2008.02.029.
[19] R. Dollevoet, Design of an Anti Head Check Profile Based on Stress Relief (Ph.D. thesis), 2010, p. 151, http://dx.doi.org/10.3990/1.9789036530736.
[20] A.C. Athukorala, D.V.D. Pellegrin, K.I. Kourousis, Characterisation of head-hardened rail steel in terms of cyclic plasticity response and microstructure for improved material modelling, Wear 366–367 (2016) 416–424, http://dx.doi.org/10.1016/j.wear.2016.03.024.
[21] O. Hajizad, A. Kumar, Z. Li, R.H. Petrov, J. Sietsma, R. Dollevoet, Influence of microstructure on mechanical properties of bainitic steels in railway applications, Metals 9 (7) (2019) 778, http://dx.doi.org/10.3390/met9070778.
[22] M. Naeimi, Z. Li, R.H. Petrov, J. Sietsma, R. Dollevoet, Development of a new downscale setup for wheel-rail contact experiments under impact loading conditions, Exp. Tech. 42 (1) (2017) 1–17, http://dx.doi.org/10.1007/s40799-017-0216-z.
[23] P. Zhang, J. Moraal, Z. Li, Design, calibration and validation of a wheel-rail contact force measurement system in V-Track, Measurement 175 (2021) 109105, http://dx.doi.org/10.1016/j.measurement.2021.109105.
[24] P. Zhang, Z. Li, Experimental study on the development mechanism of short pitch corrugation using a downscale V-Track test rig, Tribol. Int. 180 (2023) 108293, http://dx.doi.org/10.1016/j.triboint.2023.108293.
[25] J.J. Kalker, Three-Dimensional Elastic Bodies in Rolling Contact, Springer Netherlands, 1990, URL https://www.ebook.de/de/product/2225648/j_j_kalker_three_dimensional_elastic_bodies_in_rolling_contact.html.
[26] G. Donzella, M. Faccoli, A. Ghidini, A. Mazzù, R. Roberti, The competitive role of wear and RCF in a rail steel, Eng. Fract. Mech. 72 (2) (2005) 287–308, http://dx.doi.org/10.1016/j.engfracmech.2004.04.011.
[27] X. Zhao, Z. Li, The solution of frictional wheel–rail rolling contact with a 3D transient finite element model: Validation and error analysis, Wear 271 (1–2) (2011) 444–452, http://dx.doi.org/10.1016/j.wear.2010.10.007.
[28] Z. Yang, A. Boogaard, Z. Wei, J. Liu, R. Dollevoet, Z. Li, Numerical study of wheel-rail impact contact solutions at an insulated rail joint, Int. J. Mech. Sci. 138–139 (2018) 310–322, http://dx.doi.org/10.1016/j.ijmecsci.2018.02.025.
[29] Z. Wei, L. Z., Z. Qian, R. Chen, R. Dollevoet, 3D FE modelling and validation of frictional contact with partial slip in compression-rolling evolution, Int. J. Rail Transp. 4 (1) (2015) 20–36, http://dx.doi.org/10.1080/23248378.2015.1094753.
[30] X. Deng, Z. Qian, R. Dollevoet, Lagrangian explicit finite element modeling for spin-rolling contact, J. Tribol. 137 (4) (2015) http://dx.doi.org/10.1115/1.4030709.
[31] S. Li, M. Naeimi, C. He, R. Dollevoet, Z. Li, An integrated 3D dynamic FE vehicle-track model in elasto-plasticity to investigate short pitch corrugation under cyclic wheel loads, Structures 53 (2023) 1000–1011, http://dx.doi.org/10.1016/j.istruc.2023.05.001.
[32] F. Ren, Z. Yang, Z. Li, An efficient 3D finite element procedure for simulating wheel–rail cyclic contact and ratcheting, Tribol. Int. (2024) 109878, http://dx.doi.org/10.1016/j.triboint.2024.109878.
[33] R.v. Mises, Mechanik der festen körper im plastisch- deformablen zustand, Nachr. Ges. Wiss. Göttingen, Math.-Phys. Kl. 1913 (1913) 582–592, URL http://eudml.org/doc/58894.
[34] J. Chaboche, Time-independent constitutive theories for cyclic plasticity, Int. J. Plast. 2 (2) (1986) 149–188, http://dx.doi.org/10.1016/0749-6419(86)90010-0.
[35] S. Andersson, Friction and wear simulation of the wheel–rail interface, in: R. Lewis, U. Olofsson (Eds.), Wheel–Rail Interface Handbook, Elsevier, 2009, pp. 93–124, http://dx.doi.org/10.1533/9781845696788.1.94.
[36] M.S.D. Sakhamuri, T.J. Harvey, B. Vierneusel, R.J.K. Wood, Wear induced changes in surface topography during running-in of rolling-sliding contacts, Wear 522 (2023) 204685, http://dx.doi.org/10.1016/j.wear.2023.204685.
[37] C. Esveld, The rail, in: D.Z. van Nieuwhuizen (Ed.), Modern Railway Track, second ed., MRT productions, 2001, pp. 275–332.
[38] S.M. Hasan, D. Chakrabarti, S.B. Singh, Dry rolling/sliding wear behaviour of pearlitic rail and newly developed carbide-free bainitic rail steels, Wear 408–409 (2018) 151–159, http://dx.doi.org/10.1016/j.wear.2018.05.006.
[39] J. Lubliner, Constitutive theory, in: Plasticity Theory, Courier Corporation, 2008, pp. 111–176.
[40] N. Ohno, J. Wang, On modelling of kinematic hardening for ratcheting behaviour, Nucl. Eng. Des. 153 (2–3) (1995) 205–212, http://dx.doi.org/10.1016/0029-5493(95)90012-8.
[41] C.L. Pun, Q. Kan, P.J. Mutton, G. Kang, W. Yan, An efficient computational approach to evaluate the ratcheting performance of rail steels under cyclic rolling contact in service, Int. J. Mech. Sci. 101–102 (2015) 214–226, http://dx.doi.org/10.1016/j.ijmecsci.2015.08.008.
[42] X. Ma, L. Wang, J. Xu, Q. Feng, L. Liu, H. Chen, A two-dimensional ordinary state-based peridynamic model for surface fatigue crack propagation in railheads, Eng. Fract. Mech. 265 (2022) 108362, http://dx.doi.org/10.1016/j.engfracmech.2022.108362.
[43] Z. Zhou, W. Li, Z. Wen, S. Zhou, G. Tao, Three-dimensional elastic–plastic stress analysis of wheel–rail cyclic rolling contact using finite element method, Wear 542–543 (2024) 205277, http://dx.doi.org/10.1016/j.wear.2024.205277.
[44] C. He, Z. Yang, P. Zhang, S. Li, M. Naeimi, R. Dollevoet, Z. Li, A finite element thermomechanical analysis of the development of wheel polygonal wear, Tribol. Int. 195 (2024) 109577, http://dx.doi.org/10.1016/j.triboint.2024.109577.
[45] Y. Yang, R. Wang, J. Wang, L. Ling, K. Wang, W. Zhai, Comparison of wheel/rail contact modelling in prediction of wheel tread wear under changeable friction conditions, Veh. Syst. Dyn. (2024) 1–30, http://dx.doi.org/10.1080/00423114.2024.2424292.